Additive Manufacturing Letters 3 (2022) 100083

Contents lists available at ScienceDirect

Additive Manufacturing Letters

journal homepage: www.elsevier.com/locate/addlet

Short Communication

3D tracking velocimetry of L-PBF spatter particles using a single high-speed plenoptic camera

Ralf D. Fischer[a,1,*], Mahyar Moaven[b,1], Dustin Kelly[b], Sarah Morris[b], Brian Thurow[b], Barton C. Prorok[a]

[a] Auburn University, Materials Research and Education Center, Auburn, AL, USA
[b] Auburn University, Advanced Flow Diagnostics Laboratory, Auburn, AL, USA

ARTICLE INFO

Keywords:
Additive Manufacturing
Spatter
Laser-Powder Bed Fusion
Metal
Particle Tracking
High-Speed Imaging
Plenoptic Camera

ABSTRACT

Particle spatter is an unavoidable by-product of the Laser-Powder Bed Fusion (L-PBF) process, as the high intensity of the incoming laser beam generates high vapor fluxes on the meltpool, allowing metal particles to be ejected into the process environment. This is detrimental to the final manufactured part, as it risks the incorporation of defects. It is therefore important to study this spattering behavior and to apply the knowledge gained to further improve the L-PBF process. This work introduces the use of a high-speed plenoptic camera to acquire 3D spatter particle trajectories generated via L-PBF line tracks. Spatter particles are tracked in the volume above the laser-metal interaction zone at 1000 fps and their velocity calculated. It is found that the calculated speeds of the spatter particles are within the expected range for this process, and that the behavior is a complex 3-dimensional process.

1. Introduction

Among the additive manufacturing technologies, Laser-Powder Bed Fusion (L-PBF) has become the dominant technique to fabricate metal parts with intricate features [1,2]. However, consistently achieving a high quality of the printed part is a challenge. Defects generated during the L-PBF process can lead to a degradation of mechanical properties and create uncertainties on the reliability of final parts. This significantly impacts the utilization of L-PBF in various industries such as aerospace, energy, and biomedical [3]. Spatter is a main contributor to defect generation and is currently unavoidable during L-PBF because it is inherent to the process itself [4,5]. The high-intensity laser irradiation causes the formation of a vapor plume, which develops a low-pressure zone next to the scan track. This low-pressure zone can entrain surrounding particles, leading to a denudation zone [6,7]. Furthermore, the recoil force exerted onto the melt pool can become strong enough to overcome the compressive surface tension of the liquid, creating a depression and ejecting hot metal spatter [4,8,9]. This can compromise the integrity of the part by (a) reducing the available material of succeeding layers, (b) potentially deflecting the incoming laser beam, (c) picking up oxygen from the process environment during its time of flight, and (d) accumulate material leading to significant increases in particle size and changes to the morphology and shape of the particles [4,5,10–14]. As such, it is important to study spatter trajectories and velocities in L-PBF to develop and assess methods to reduce the incorporation of spatter into the final part.

Current strategies to reduce the amount of incorporated spatter include tailoring the process and scanning parameters [14–16], environmental conditions [7,10] and the introduction of cross gas flow across the build area [17,18]. Optical techniques such as shadowgraphy [8,10], visible light [5,18], infrared light [9] and X-ray high-speed imaging [19,20] have been used to understand the spatter formation and trajectory. However, these measurements are limited to a 2D plane of a complex 3D process. As such, methods to capture the spatter particles in a 3D volume need to be adopted. One such approach is the use of tomographic particle tracking velocimetry (PTV), where four or more cameras are aimed at the space above the interaction zone at different angles, allowing for the capture of both the 3D location and velocity of particles [21,22]. However, tomographic PTV can be financially and spatially prohibitive as it not only requires the acquisition of multiple high-speed cameras, but also requires multiple optical access points to the chamber, which can be very difficult or impossible in commercial units.

A solution to the constraints of traditional tomographic imaging is the use of light-field imaging to acquire 3D information. While traditional imaging techniques only record a 2D projection of the distribution of light intensities, light-field imaging simultaneously acquires spatial, angular, and spectral information from a scene. An

* Corresponding author.
E-mail addresses: rfischer@auburn.edu (R.D. Fischer), thurobs@auburn.edu (B. Thurow), prorobc@auburn.edu (B.C. Prorok).
[1] These authors contributed equally.

https://doi.org/10.1016/j.addlet.2022.100083
Received 21 June 2022; Received in revised form 24 July 2022; Accepted 30 July 2022

effective instrument for light-field imaging is the plenoptic camera, which captures a subset of the light-field by acquiring spatial and angular information. The modern concept of plenoptic imaging was derived by Adelson and Wang [23] and the first plenoptic 1.0 hand-held camera was developed by Ng et al. [24], where a microlens array was placed a focal length away from the sensor of a traditional camera. The main lens focuses light onto the microlens array which splits up light rays based on their angle of incidence with the main aperture plane. These rays subsequently intersect the imaging sensor, thus encoding 3D information of a captured scene into raw plenoptic images. With the appropriate selection of pixels behind each microlens, a plenoptic camera is capable of performing perspective shifting across the aperture and computational refocusing through an imaged volume. Recently, Tan et al. [25] developed a modular plenoptic camera to increase temporal resolution compared to previous plenoptic cameras.

This work introduces the use of a high-speed plenoptic camera to obtain 3D location tracking and velocimetry of spatter particles during the L-PBF process. Accurate 3D spatter data acquisition can be used to support research efforts to develop methods to mitigate the impact spatter particles have on the quality of additively manufactured parts. The plenoptic camera is designed to collect angular information from incoming light rays such that the 3D position of an object can be retrieved. Key advantages of this system include its low requirement for optical access and simplicity in experimental data acquisition; rather than setting up four or more cameras to acquire 3D information, as is typically the case in 3D-PTV experiments, a single plenoptic camera is used to triangulate the position of spatter particles. A primary challenge in 3D particle imaging is the determination of an individual particle's location on each camera in the system; as the number of particles increases, matching particles between different cameras becomes increasingly challenging, resulting in ghost particles whereby images belonging to two different particles are used for triangulation thus producing a non-physical location [26]. A common solution is to add more cameras to reduce this ambiguity; however, the abundance of views provided by the plenoptic camera result in the issue of ghost particles being greatly reduced as compared to traditional camera experiments. The present work focuses on 3D-location tracking velocimetry of spatter particles in the L-PBF process.

2. Materials and methods

2.1. Experimental setup

In this work, single line experiments were performed on an L-PBF test bed. The optical system consists of an IPG YLR-400AC continuous wave ytterbium fiber laser with a wavelength of 1070 nm and a maximum output power of 400 W. The laser beam is delivered using an IPG Mid-Power Scanner with a 250 mm f-theta lens, resulting in a Gaussian power profile and a focal spot size of approximately 100 μm (M^2 = 1.1). The optical system is attached to a chamber with displacement control of the coater, build plate and powder reservoir as shown in Fig. 1. For the purpose of demonstrating the capabilities of the camera, experiments were conducted in ambient air conditions and without gas flow across the build plate.

Inconel 625 was used as a base material for both the powder as well as the substrate because of its wide use in L-PBF and its low oxygen susceptibility allows for safe handling in ambient conditions [27]. The particle size of the powder is between 15 and 45 μm. The substrate was ground flat with up to 1000 grit grinding paper. A 25 μm powder layer was spread on the substrate. The specimen was placed within the chamber underneath the scanner and the height was adjusted such that the interaction zone was within the focal plane.

The plenoptic camera used in the experiments, shown in Fig. 2, is a variation of the high-speed plenoptic camera first introduced by Tan et al. [25]. It consists of a Phantom VEO4k high-speed camera, a 471 × 362 microlens array housed in a relay assembly, a 350 mm focal length collimating lens, and a 150-mm focal length focusing lens. While conventional plenoptic cameras have a microlens array mounted directly in front of the camera sensor, the modular plenoptic camera used in this work relays the microlens images to the sensor. A relay system consisting of four, two inch diameter, 150 mm focal length achromatic doublets was developed to minimize chromatic aberrations. The use of a relay system results in a larger form factor that could be significantly reduced via integration of a microlens array a small distance in front of the sensor. Further details about the setup are provided in Table 1. This configuration resulted in a magnification of -0.62, allowing for a field of view of 22.4 × 22.4 mm, a depth of field of approxi-

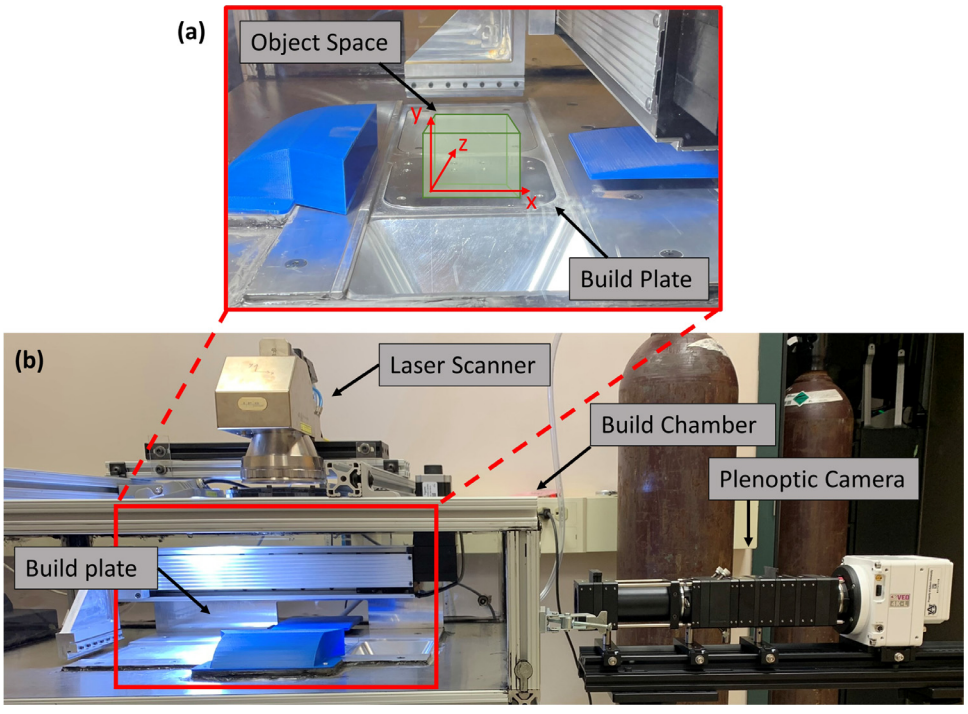

Fig. 1. (a) Build chamber of the L-PBF test bed showing the build plate and the object space from the viewpoint of the plenoptic camera. (b) Side view of the experimental setup showing the Build chamber and the optical module as well as the plenoptic camera.

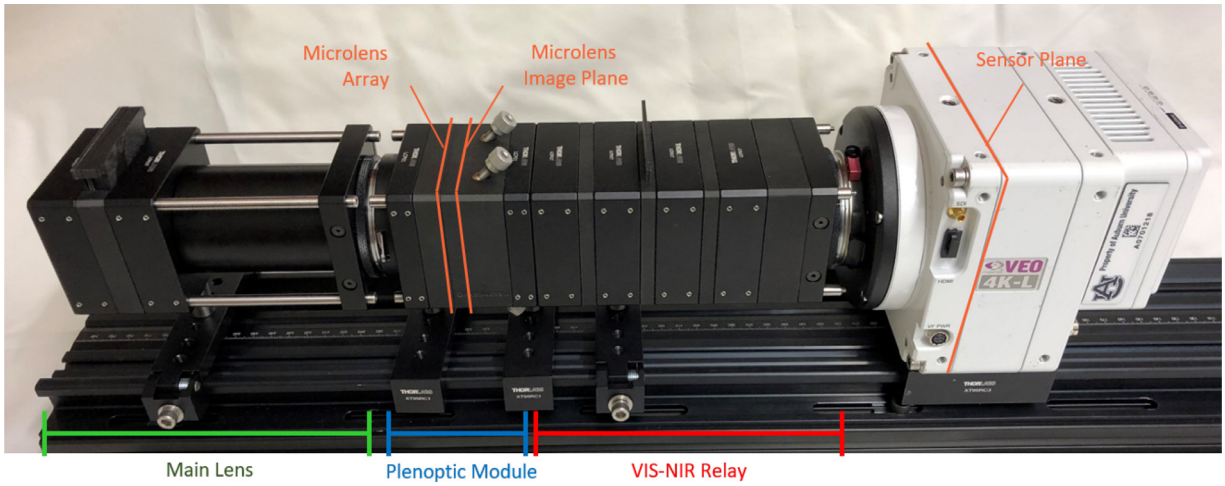

Fig. 2. The high-speed modular plenoptic camera with labeled components.

Table 1
High-speed spectral plenoptic camera specifications.

Parameter	Value	Parameter	Value
Camera	Phantom VEO4k	Microlens Type	Hexagonal
Microlens Pitch	0.077 mm	Pixel pitch	0.00675 mm
Microlens focal length	0.308 mm	Number of pixels: X-direction	4096
Microlens f-number	4	Number of pixels: Y-direction	2304
Number of microlenses: X-direction	471	Lens 1 focal length	350 mm
Number of microlenses: Y-direction	362	Lens 2 focal length	150 mm

mately 50 mm, and estimated uncertainties at the nominal focal plane of 0.17 mm and 1.72 mm in the in-plane ($x-y$) and out-of-plane (z) directions, respectively [28]. Images were captured at 1000 fps with a resolution of 2048 × 2048 pixels and an exposure time of 90 µs. The spatter particles produce self-emitted radiation as a result of their high temperature, and thus external illumination sources are not necessary.

The coordinate system is chosen relative to the plenoptic camera, see Fig. 1(a). The $x-y$ plane is parallel to the image plane and the z-axis is parallel to the optical axis of the camera. The origin of the coordinate system is placed at the bottom left corner of the image plane and the center of the focal plane of the camera. The object space is approximately 3 mm above the interaction zone.

Single track experiments representing typical exposures during the L-PBF process were conducted along the x-axis, meaning that specimen and laser tracks were placed at the nominal focal plane of the camera. To run multiple experiments, the substrate was moved along the z-axis between single track experiments while the laser scanner and camera were held stationary such that the scan vector is independent of the position of the substrate plate. Two different exposure experiments were performed: (1) a single line laser track at 600 mm/s and 200 W laser power and (2) a turnaround laser track at 600 mm/s, 200 W laser power and an 80 µm offset or hatch distance.

2.2. Methodology - 3D particle tracking velocimetry

The image processing flow chart taken from plenoptic image acquisition to 3D spatter particle velocimetry is shown in Fig. 3 and discussed below. In brief, a stack of perspective images is generated by sampling the same pixel under each microlens, relative to the microlens centers. This creates views of the spatter particles from multiple discretized locations on the main lens plane (u, v). Identifying particle positions in these perspective images yields their location of projection on the microlens plane (s, t). As a result, particle images can be characterized by rays extending from the main lens to the microlens plane ((u, v) to (s, t)). Particle rays from different perspectives are then grouped via a bundling algorithm such that each bundle ideally includes all the available rays for a single particle and each ray corresponds to the view of that particle from a unique perspective. 3D positions are subsequently obtained by way of an image to object space mapping function. Finally, an adapted tracking scheme links particles together through time, enabling velocity and other properties associated with particle positions to be determined. The total computation time to obtain spatter velocities from plenoptic images is approximately 10 minutes on a modern desktop computer.

2.2.1. Plenoptic decoding

Plenoptic imaging typically involves decoding raw images into perspective images based on discrete positions (u, v) on the main lens plane. The microlenses capture sub-aperture images while refracting incoming rays based on their angle of incidence with the main lens (Fig. 4). Perspective images are generated by selecting from each microlens a pixel whose position relative to the microlens center corresponds to the desired (u, v) location. These can be considered as different viewpoints of the scene, thus providing angular information crucial to recovering the depth of an imaged particle. The spatial resolution of a perspective image is relative to the number of microlenses imaged by the sensor, which was 112 × 130 for this effort. A prerequisite to this step involves capturing a reduced aperture image of a white background in order to find the center of projection of each microlens on the image sensor (see Fahringer et al. [29] for further information).

2.2.2. Particle identification

First, Light-Field Ray Bundling (LFRB) searches through each perspective image for particle candidates. Particle identification was performed using a dynamic threshold segmentation (DTS) algorithm available as part of the open-source Prana package [30]. DTS operates by isolating local intensity peaks while eroding surrounding pixels and subsequently performing an iterative dilation to deduce which pixels belong to each particle. A key advantage of DTS is its exceptional ability to distinguish particles from background noise; however, if the intensity of a particle's image drops to levels comparable to that of background noise, it may not be identified. Additional reasons for a particle being unidentified include view-based occlusions (such as overlapping of particles) and

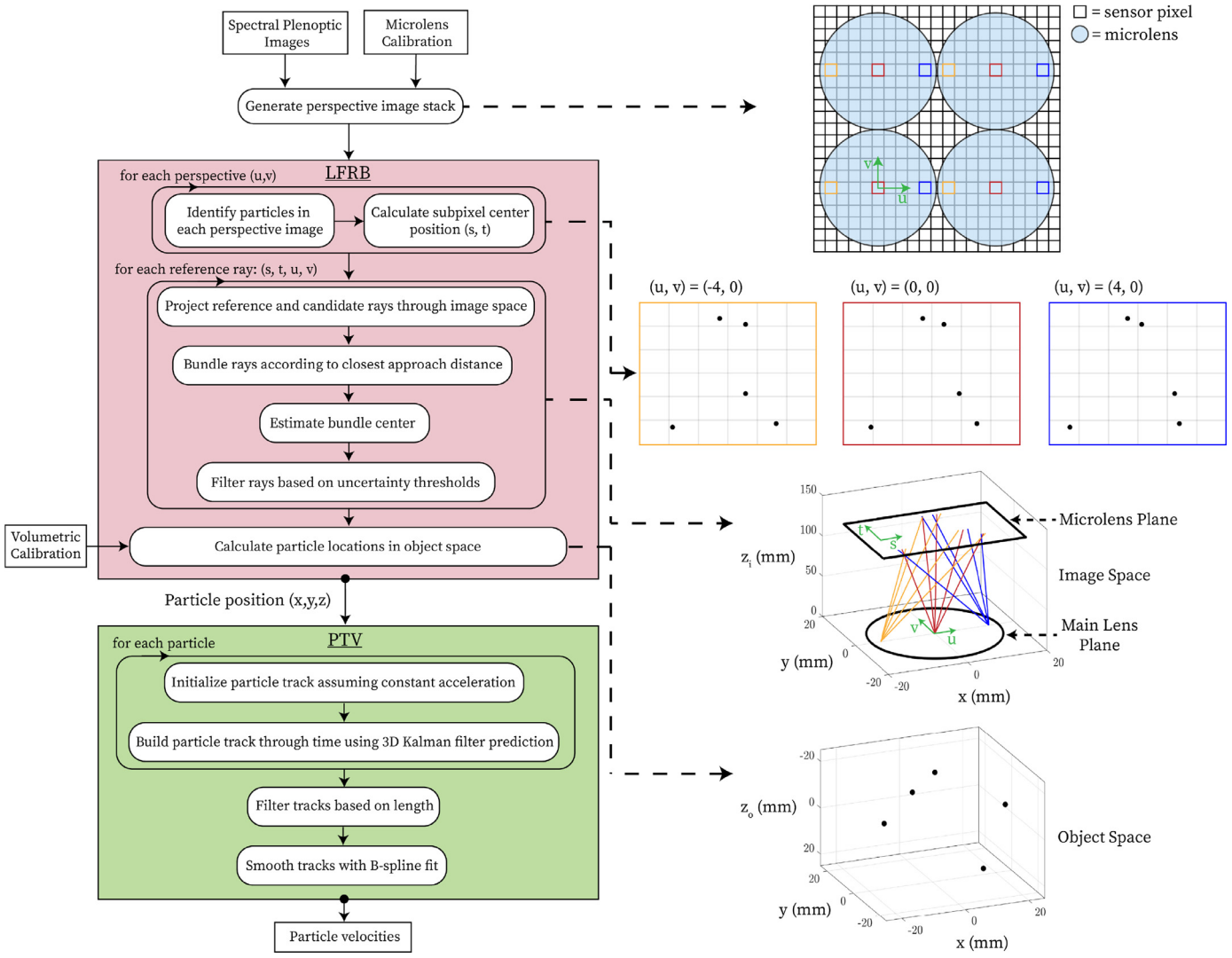

Fig. 3. Flow chart of Light-Field Ray Bundling (LFRB) and PTV starting from image acquisition to extracting spatter particle velocities. Note that z_i and z_o in the bottom-right plots refer to depths in image and object space, respectively.

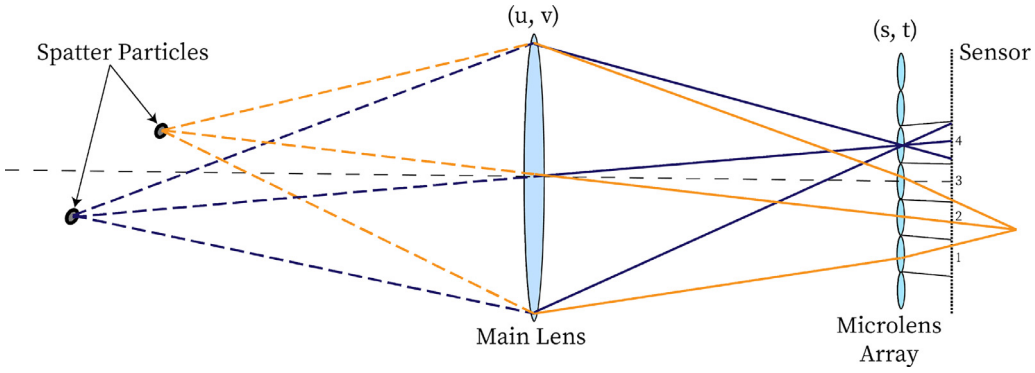

Fig. 4. Ray-tracing diagram for plenoptic (1.0) imaging.

vignetting. These effects are largely mitigated by the plenoptic camera's ability to generate multiple perspective views of a scene; for example even if a particle is occluded in some central perspectives, it will be visible in outer perspective views provided no other obstructions are present. After particle candidates are found, their subpixel center positions are calculated by applying a weighted centroid scheme around the peak pixel, which is typically accurate to less than 0.1 pixels [31].

The detectability of a particle on the sensor is a function of size, temperature, emissivity, and 3D location. With relation to size, and keeping other variables constant, the intensity of a particle is proportional to surface area (r_2 for spherical particles). With the current camera bit-depth of 12 and dynamic range of 9 stops, the ratio between largest to smallest detectable particle radii is approximately 22. Although not implemented in this effort, a potential for future work could be to dis-

tinguish between different types of spatter based on size, which can be determined by projecting the spatter image into object space using magnification. This is contingent on the spatter image exceeding the size of a perspective image pixel in object space (62.2 μm).

2.2.3. Ray projection

The subpixel center position on each perspective image represents the intersection of that ray with the microlens plane and is denoted by $(s,\ t)$. The distance (z_i) between the main lens and microlens planes can be approximated by applying the thin lens assumption, which projects rays assuming a lens thickness negligible in comparison to its radius of curvature. At this stage, all the information required to form a parametric equation representing a ray in image space intersecting these two planes is known (solid lines in Fig. 4) [32]. Assuming a particle is identified in N_{uv} perspective views, there will be up to N_{uv} two-plane parametrizations (i.e. rays) for that particle.

2.2.4. Sorting rays

As the identification of particles is independent across perspective views, LFRB aims to sort particle rays into bundles such that each bundle consists of rays projecting from a single particle. For more details on this process, the authors refer the reader to work by Clifford et al. [33]. Beginning with a reference ray $(\vec{a})$ in the first perspective, a candidate ray $(\vec{b})$ is selected from a different perspective. Between these two particle rays exists a line of closest approach whose length, d, is calculated by the following equation:

$$d = \left| \frac{(\vec{p}_B - \vec{p}_A) \cdot \vec{n}}{\vec{n} \cdot \vec{n}} \right| \tag{1}$$

where $\vec{p}_A$ and $\vec{p}_B$ are the intersection points of $\vec{a}$ and $\vec{b}$ with the microlens plane, respectively, and $\vec{n} = \vec{a} \times \vec{b}$. Eq. (1) is applied to every remaining ray in the perspective image and the particle rays are sorted by their length. The candidate ray corresponding to the shortest line of closest approach is selected and the length of the line is filtered against a user-defined maximum distance threshold. If the length is below the threshold, the candidate ray is indexed as belonging to the same bundle as the reference ray. At this stage, the endpoints of the closest approach line are calculated:

$$\vec{p}_{A|B} = [u_A, v_A, 0]' + \frac{(\vec{b} - \vec{a}) \cdot \vec{n}_B}{\vec{a} \cdot \vec{n_B}} \cdot \vec{a} \tag{2}$$

$$\vec{p}_{B|A} = [u_B, v_B, 0]' + \frac{(\vec{a} - \vec{b}) \cdot \vec{n}_A}{\vec{b} \cdot \vec{n_A}} \cdot \vec{b} \tag{3}$$

where (u_A, v_A) and (u_B, v_B) represent perspective view coordinates corresponding to each ray, $\vec{n}_A = \vec{a} \times \vec{n}$, and $\vec{n}_B = \vec{b} \times \vec{n}$. An estimate of the bundle center in image space, corresponding to the points of convergence of the solid lines in Fig. 4, can now be made by taking the average of these endpoints. This procedure is repeated across every remaining perspective such that each perspective view adds a maximum of one ray to the reference ray's bundle while updating the estimated bundle center position. The tightness of the bundle core is now checked against a radius and elongation threshold obtained by multiplying estimations of uncertainty associated with plenoptic imaging (based on equations derived by Deem et al. [28]) in the in-plane and out-of-plane directions, respectively, by a constant factor (1.5 used for this dataset). If the in-plane distance between the approximated center and the endpoint of a ray's closest approach line exceeds the bundle radius threshold or the out-of-plane distance exceeds the bundle elongation threshold, the ray in question is considered to have been grouped with the incorrect reference ray and is consequently removed from the bundle. After filtering, if a bundle is comprised of a number of rays exceeding a user-defined percentage of the number of generated perspectives (i.e. maximum number of rays for a particle) it is considered a particle otherwise it is deemed likely to be made up of noise, image artefacts, or a selection of misbundled particle rays. Note that particle rays accepted into a bundle are removed from the pool of candidate rays to prevent duplications across multiple bundles. The inner loop of the sorting algorithm cycles through the above steps taking each ray in the first perspective as a reference ray. After this is done, any leftover particle rays in the next perspective are used as reference rays and thus the outer loop runs through each perspective until every ray is either bundled or considered as a reference ray to which others are bundled.

2.2.5. Calibration

Rays from each particle have been sorted into bundles in image space but require an image to object space transformation in order to find the particle's position in the 3D volume. This necessitates calibration of the optical system to the imaged volume, which was achieved here by performing direct light-field calibration [34]. A checkerboard-patterned calibration plate was mounted onto a Thorlabs 300 mm linear translation stage and imaged while traversed through the volume in 3 mm increments across a 42 mm depth. Raw images were decoded into 48 perspective images (u, v) and the checkerboard's corner points (s, t) were identified in each image. With the dimensions of the checks known (3 × 3mm), every corner point is assigned (x, y, z) coordinates based on its position on the checkerboard and the depth. A generic polynomial mapping function is employed to relate 2D image positions to 3D world coordinates across each perspective image, thus encoding angular information:

$$s = F(x, y, z, u, v, s_c) \tag{4}$$

$$t = F(x, y, z, u, v, t_c) \tag{5}$$

where s_c and t_c are coefficients in the s and t directions, respectively, and are calculated using a least-squares approach.

2.2.6. Triangulation

A set of (x, y, z) coordinates for each particle is solved for such that the distance between the output of the calibration function and detected particle positions (s_p, t_p) on the sensor are minimized in a nonlinear least-squares fashion:

$$min \sqrt{(s_p - F(x, y, z, u, v, s_c))^2 + (t_p - F(x, y, z, u, v, t_c))^2}. \tag{6}$$

Triangulating the object space position of every bundled set of particle rays provides a list of 3D particle positions for each image. An estimate of the accuracy of particle positions obtained from LFRB is given by Clifford et al. [33], where the authors found an error of 0.07 mm at a magnification of -0.5 using synthetic single-particle plenoptic images. The remainder of this section will focus on the steps necessary to track these particles through time.

2.2.7. Track initialization

A four-frame tracking approach based on the four-frame best estimate–enhanced track initialization (4BE-ETI) technique was adapted to this experiment [35]. Note that a modification to the algorithm to increase its robustness for this application was applied whereby the initial search box was offset by a user-defined global prediction of particle displacement. As a visual aid for the following explanation, refer to the 2D illustration of Fig. 5. For a given particle $Q_{A_{\tau 0}}$ at $(x_A,\ y_A,\ z_A,\ \tau_0)$, consider all particles within a search box around $(x_A + dx,\ y_A + dy,\ z_A + dz)$ at time:

$$\tau_1 = \tau_0 + \Delta\tau. \tag{7}$$

as potential matches, where $(dx,\ dy,\ dz)$ are user-defined initial predictions of displacement. Now for each candidate particle at τ_1, assume a constant velocity from $Q_{A_{\tau 0}}$ to predict positions at:

$$\tau_2 = \tau_0 + 2\Delta\tau. \tag{8}$$

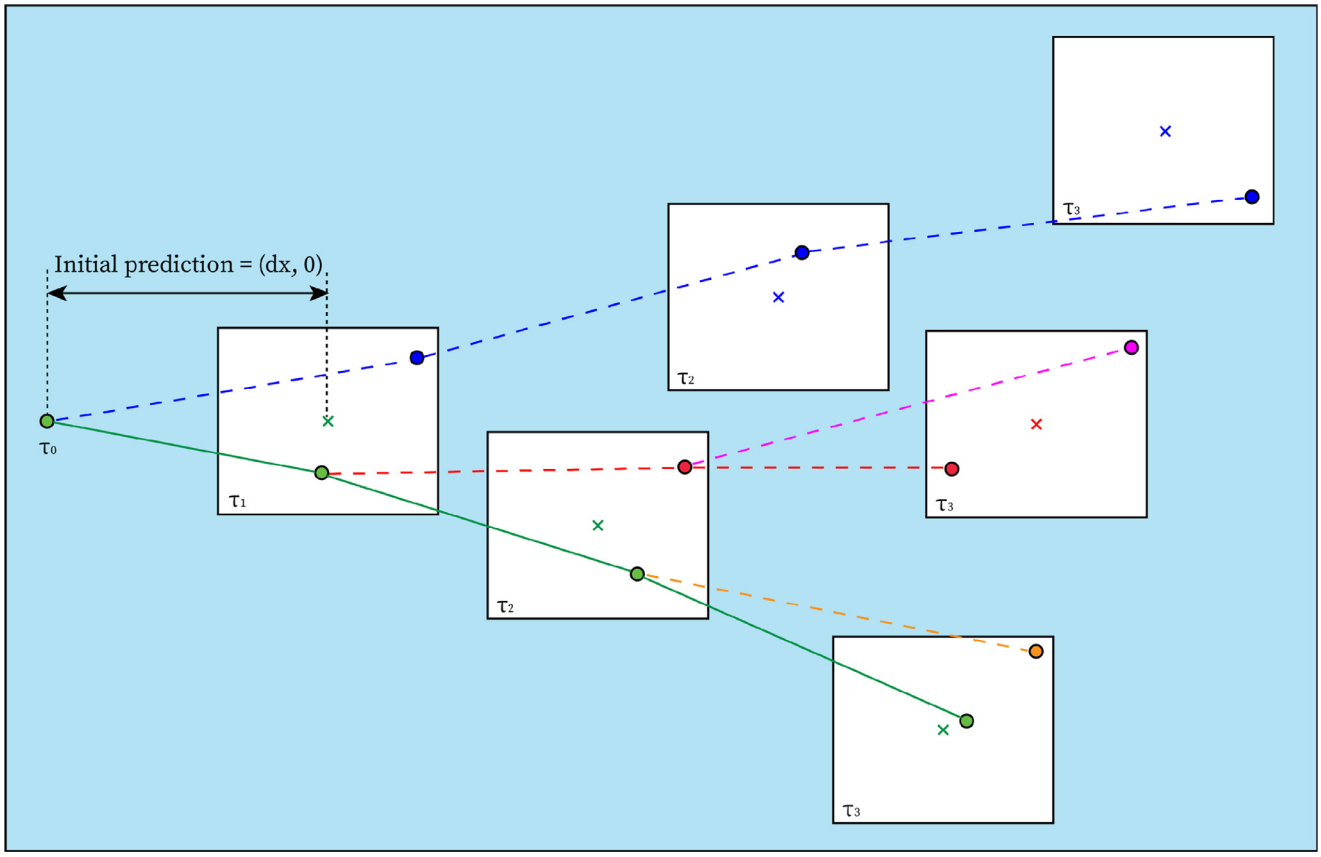

Fig. 5. A 2D illustration of the adapted 4BE-ETI algorithm used in this work, inspired by Fig. 1 of Clark et al. [35]. Crosses represent predicted positions based on the particle of the same color from the previous time-step. Dashed lines show links to potential matching particles within the search boxes while solid lines represent the accepted track after minimizing acceleration across all four images.

Again, particles in each search box are considered candidates for that track. A constant acceleration from τ_0 to τ_2 is assumed in order to predict particle positions at:

$$\tau_3 = \tau_0 + 3\Delta\tau. \tag{9}$$

Any particles in the search box around the predicted position at τ_3 complete each of their respective four-frame tracks. For each particle track, the change in acceleration is calculated and the track corresponding to the minimum change is selected as the most probable. This method implies that the maximum velocity obtainable after spatter ejection is such that the spatter has to be captured within the camera's imaging volume for four consecutive frames.

2.2.8. Spatter tracking

A 3D Kalman filter is fit to each particle track to help provide an estimate for the next point in the track ($\tau + \Delta\tau$) and if particles are found within a search box around the prediction, the closest candidate is added to the particle track. The Kalman filter state is then updated with the selected particle position. If no candidates are found within the search box, the prediction point is stored as a pseudoparticle from which a prediction can be made to the subsequent time point ($\tau + 2\Delta\tau$). This means if a particle is not identified in one image (e.g. due to intensity drop) but reappears in the next, it can still be tracked. A particle track is only allowed to hold a pseudoparticle for a maximum of one time step and is ended if no subsequent particles are found. Any particle track lasting less than three time instances is assumed to be unreliable and/or consist of erroneously bundled particles, caused in this case by image artifacts, and is deleted. Assuming particles are linked correctly between images, the accuracy of obtained velocities is dependent on the particle position error. As such, tracks are smoothed with a fourth order B-spline—a common measure in PTV to mitigate effects of uncertainty in position estimation [36]. Finally, the instantaneous 3D velocity of each particle is calculated by taking the difference in its position across consecutive time points: $V = (Q_{i_{\tau(n+1)}} - Q_{i_{\tau(n)}})/\Delta\tau$.

3. Results and discussion

Spatter particles resulting from the L-PBF process were successfully tracked using the high-speed plenoptic camera. The camera was operated at 1000 fps, capturing 50 images for the turnaround track and 170 images for the continuous track, where in the latter only the first 72 images were used for particle tracking. A plenoptic image of particles from the turnaround case is shown in Fig. 6. The reader is referred to Supplementary Information S1 and S2 for the original high-speed videos of the turnaround and single line laser track, respectively. The location of each particle was calculated using LFRB for each image and velocimetry was conducted using a 3D Kalman filter across the series of images.

Particle tracks for the turnaround laser track were obtained over the 50 images and are shown in Fig. 7. For visual clarity, only one in three particle tracks is displayed. Throughout the time frame of the turnaround laser track, 1135 particle locations were found. 798 data points could be fitted to 107 corresponding particle tracks, while the remaining 337 data points could not be assigned particle tracks or got filtered out due to insufficient information. Similarly, 1333 particle locations were found in 72 images for the continuous laser track, where 603 locations could be assigned to 84 particle tracks, leaving the remaining 730 data points unassigned or filtered out. Supplementary Information S3 and S4 show the 3D-tracking of the particles throughout the time frame for the turnaround and continuous laser track, respectively.

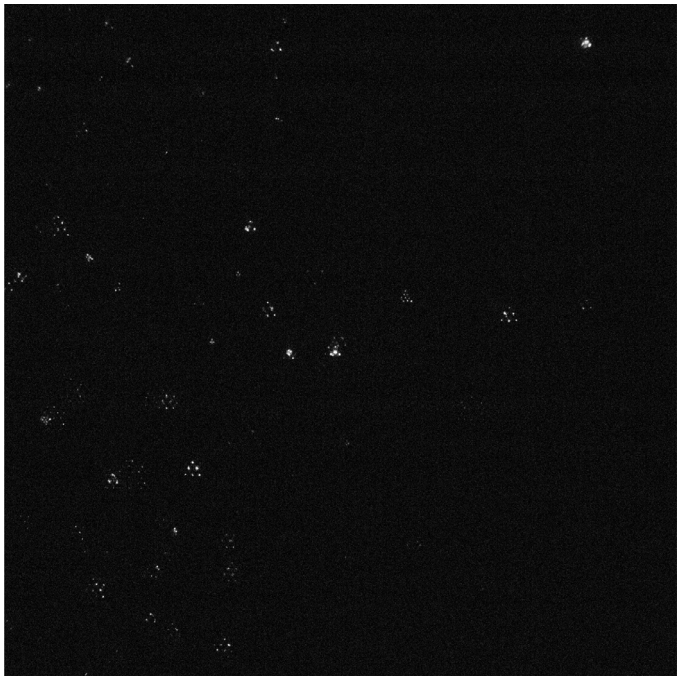

Fig. 6. Raw plenoptic image of spatter particles.

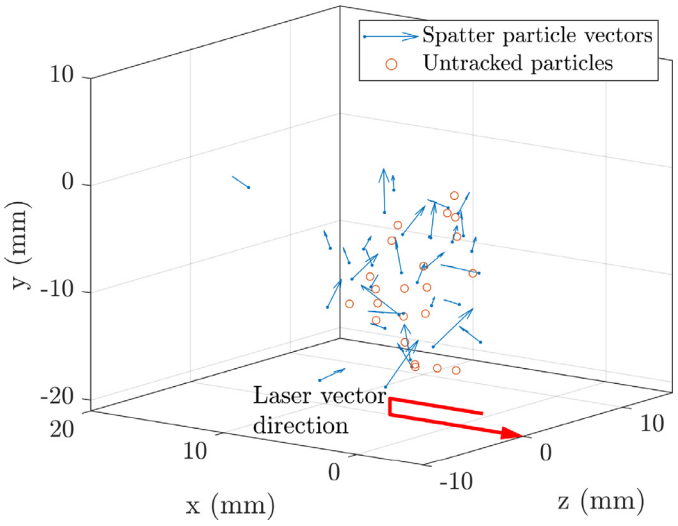

Fig. 8. Spatter distribution after the turnaround point at image 18.

Fig. 8 shows the reconstructed position of the spatter particles detected from an image right after the turnaround of the laser track in image 18. In this image, the algorithm was able to track 34 particles of a total of 55 particles detected. The velocity and trajectory can be identified by the length and orientation of the blue arrows, respectively. Of the remaining particles, nine were not able to be tracked and twelve were filtered due to their respective track's insufficient length. The locations of these particles are displayed as red circles. The particle trajectories are dominated by vertical motion away from the melt pool. Because the trajectories are determined in 3D, particle velocities can be separated into their three relative components. This reveals that the particles are not only ejected up and back, but also have a significant component towards the sides. The high velocities of 1.3 m/s in the y-direction and 0.8 m/s in the z-direction lead to an angle of propagation of the spatter particles of 88.4° around the x-axis. The high velocities observed to the side of the laser track reveals the complex 3D nature of spattering during the L-PBF process.

Histograms of the average speed considering all three directions of the tracked particles can be seen in Fig. 9. The average velocities of the particle tracks are 2.0 ± 1.2 m/s and 1.3 ± 1.0 m/s for the turnaround and the single line laser track, respectively. The lowest and highest recorded velocities are 0.5 m/s and 5 m/s, respectively. The velocities of spatter during L-PBF varies widely, which can be attributed to differences in the laser power, scan speed or environment, as shown in Table 2. However, velocity results are well within the expected range, demonstrating the effectiveness of this technique for 3D spatter particle tracking. An explanation for the deviation of some of the reported values can be given by the size of the spatter particles and a difference in process parameters, such as laser power, laser velocity or layer thickness.

The velocities of the particles were recorded over the duration of the experiments, as shown in Fig. 10. Interestingly, there is a sharp drop in velocity during the first millisecond, after which the velocity of the particles stabilizes to be approximately constant through the rest of the recorded time period. It is believed that the high velocity corresponds to the initial rapid ejection of particles from the melt pool.

Consistent with known limitations of plenoptic imaging, Fig. 7 shows noticeably higher deviations from a smooth trajectory in the depth direction as compared to the in-plane direction, suggesting increased uncertainty along the z-axis. Note that some particle tracks end before they

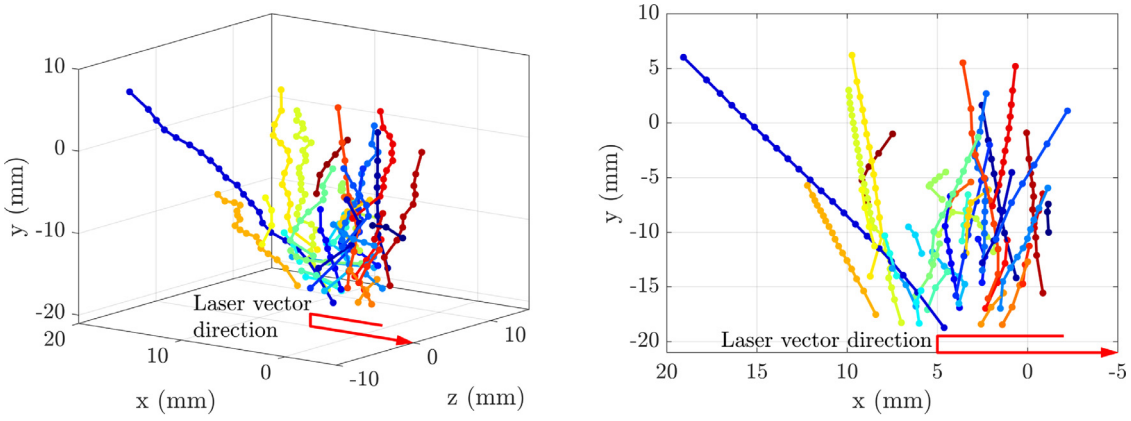

(a) **(b)**

Fig. 7. Isometric view (a) and $x-y$ plane (b) of particle tracks from the turnaround experiment (showing 1 in every 3 tracks for clarity, with different colors corresponding to different particles).

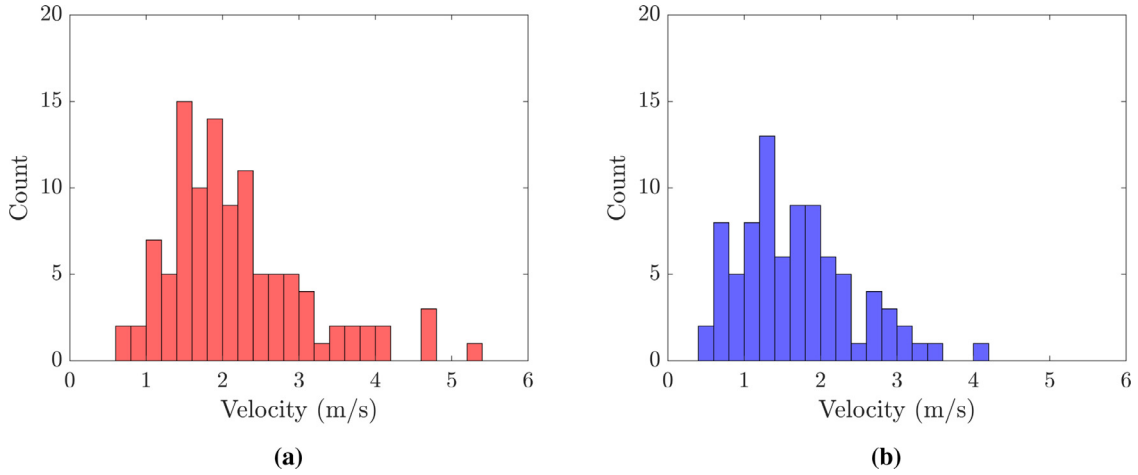

Fig. 9. Average velocity histograms of spatter particles in turnaround (a) and single line laser track (b) experiments.

Table 2
Comparison of reported particle velocities.

Ref.	Method	2D/3D	Particle velocity
This work	Plenoptic Camera	3D	2.0 ± 1.2 m/s turnaround 1.3 ± 1.0 m/s continuous
Barett et al. [37]	Stereovision	3D	0.3 – 50 m/s, 9.5 m/s mean
Gunenthiram et al. [16]	High-Speed Camera	2D	3 ± 1.5 m/s large particles 35 ± 15 m/s small particles
Yin et al. [38]	High-Speed Camera	2D	0.18 – 9.45 m/s, 3.56 m/s mean
Guo et al. [7]	High-Speed X-ray Imaging	2D	0.75 – 2.24 m/s vapor jet domain 0.27 – 0.61 m/s argon gas flow range
Pauzon et al. [10]	Shadowgraphy	2D	5.1 ± 2.6 m/s

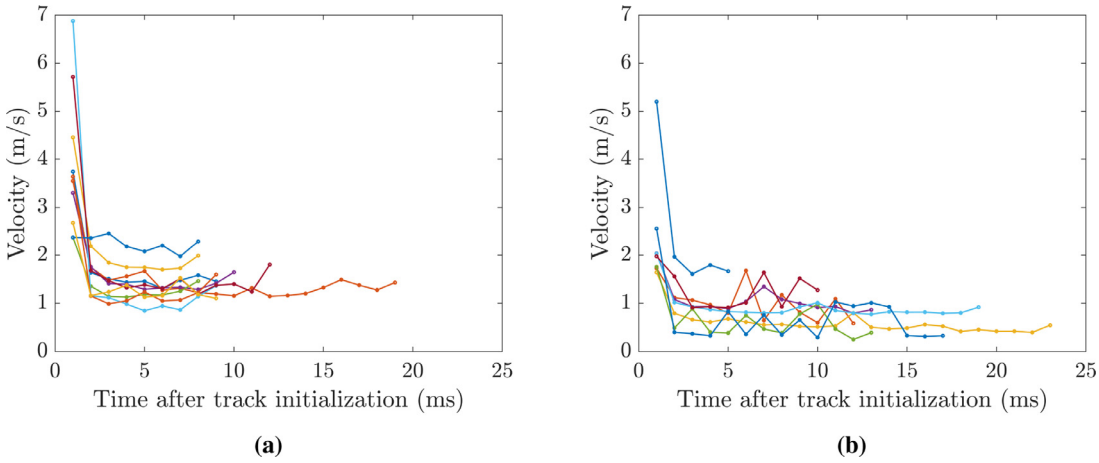

Fig. 10. Time-evolution of spatter particle velocities in turnaround laser track (a) and single laser track (b) experiments. The line colors correspond to different particle tracks.

exit the field of view, likely due to identification being hindered by particle intensities dropping close to that of background noise due to cooling particles or uncertainty in LFRB causing the reconstructed particle position to deviate from its track. Schanz et al. [36] suggested the extent of the correction of particle positions before and after track smoothing can provide a simple measure of particle position accuracy. In this experiment, particles were shifted 0.09 mm, 0.33 mm, and 0.52 mm, in the x-, y-, and z-directions, respectively. Due to limited image acquisition speed relative to spatter velocity, some particles were recorded for a time length too short for reliable tracking, therefore filtered out, potentially causing Fig. 9 to be skewed towards lower velocities. This could be rectified by using a camera with a higher frame rate or by improving the tracking algorithm.

Improvements to the particle tracking methodology is a present area of research. One method is to place the microlens array directly in front of the image sensor, thereby reducing the complexity of the optical system and leading to increased light sensitivity while minimizing chromatic aberration. Developments to the PTV code to reduce the occurrence of ghost particles and to increase robustness of particle tracks include: introducing a Shake-The-Box inspired approach where existing particle tracks are used to provide predictions for particle identification at the next time step [36], bidirectional particle tracking as opposed to stepping only forward through time, and tuning the smoothing function according to the levels of noise in each experiment. The image acquisition rate with the current system is not sufficient to allow the PTV algorithm to track collisions of spatter. However, as the high-speed plenoptic

system is modular, this could be easily addressed in the future by replacing the main camera with one capable of higher frame rates. Similarly, the spatial resolution of perspective images could be improved by using a microlens array with smaller microlenses. Although this would result in lower angular resolution, an alternative variation of the plenoptic system, termed plenoptic 2.0, results in a less severe tradeoff between spatial and angular resolution by allowing each microlens to contribute multiple pixels to a perspective image rather than just one [39]. A current limitation of the system is the detection of low light emitting particles. The addition of an illumination laser with a wavelength in the visible range will be able to resolve this. Lastly, incorporating an additional plenoptic camera has the potential to significantly improve the resolution and accuracy, especially in the z-direction.

The use of a single high-speed plenoptic camera is anticipated to have a significant impact on future studies aimed at understanding the relationship between spatter ejection, laser exposure, and environmental influences during the L-PBF process. With the knowledge of trajectory and velocity for a set scanning strategy, the cross flow of the shielding gas can be tailored to target the ejecta more effectively. This will aid in reducing the risks of incorporating spatter into the final part, therefore increasing the reliability of the fabrication method and allowing for potential flaws to be evaluated a-priori.

Furthermore, the use of a plenoptic camera allows for the incorporation of multiple spectral filters in the optical pathway, thereby differentiating intensities recorded by different wavelengths at the optical sensor. This enables temperature measurements of objects through multi-wavelength pyrometry. Enabling simultaneous location and temperature tracking can also be useful for a multitude of other applications, i.e. analyzing the melting and solidification process for directed energy deposition systems or the gas atomization process, or the analysis of the flame profiles of rocket engines.

4. Conclusion

In this work, a single high-speed plenoptic camera was introduced to observe the spattering behavior of particles during the L-PBF process. Because of the unique ability of the plenoptic camera to capture 3D information with a single camera, it can be utilized in conditions where the optical access is limited. The reconstruction algorithm was able to determine the position of spatter particles throughout the entire length of the recording and assign them particle tracks, which enable the calculation of velocity and trajectory profiles for each particle. Consistent with previous works that found plenoptic imaging uncertainty to have lower accuracy in the depth direction than in the lateral directions, greater fluctuations were observed in the out-of-plane component of spatter particle velocity relative to that of the in-plane. The data received from utilizing this method can aid in making the L-PBF process more robust by designing the material, machine layout or exposure strategies in a way that reduces the negative impacts excessive spatter can have on the final part.

Acknowledgments

Development of the modular, high-speed plenoptic system was carried out under the National Science Foundation's Major Research Instrumentation Program grant no. 1725929. The development of a custom L-PBF test bed was sponsored by the United States National Institute of Standards and Technology under contracts NIST-70NANB16H272, NIST-70NANB17H295 and NIST-70NANB18H220. The authors gratefully acknowledge the support of Mr. Steven Moore at Auburn University's Materials Research and Education Center.

Supplementary material

Supplementary material associated with this article can be found, in the online version, at doi:10.1016/j.addlet.2022.100083

References

[1] D.D. Gu, W. Meiners, K. Wissenbach, R. Poprawe, Laser additive manufacturing of metallic components: materials, processes and mechanisms, Int. Mater. Rev. 57 (3) (2012) 133–164, doi:10.1179/1743280411Y.0000000014.
[2] R.D. Fischer, J. Klasen, A. Shmatok, B.C. Prorok, An additively manufactured locking fixation system for potential application in patient-specific implants, J. Mech. Behav. Biomed. Mater. 124 (2021) 104867, doi:10.1016/j.jmbbm.2021.104867.
[3] M. Grasso, B.M. Colosimo, Process defects and in situ monitoring methods in metal powder bed fusion: a review, Meas. Sci. Technol. 28 (4) (2017) 044005, doi:10.1088/1361-6501/aa5c4f.
[4] A.N.D. Gasper, B. Szost, X. Wang, D. Johns, S. Sharma, A.T. Clare, I.A. Ashcroft, Spatter and oxide formation in laser powder bed fusion of Inconel 718, Addit. Manuf. 24 (2018) 446–456, doi:10.1016/j.addma.2018.09.032.
[5] Y. Liu, Y. Yang, S. Mai, D. Wang, C. Song, Investigation into spatter behavior during selective laser melting of AISI 316l stainless steel powder, Mater. Des. 87 (2015) 797–806, doi:10.1016/j.matdes.2015.08.086.
[6] M.J. Matthews, G. Guss, S.A. Khairallah, A.M. Rubenchik, P.J. Depond, W.E. King, Denudation of metal powder layers in laser powder bed fusion processes, Acta Mater. 114 (2016) 33–42, doi:10.1016/j.actamat.2016.05.017.
[7] Q. Guo, C. Zhao, L.I. Escano, Z. Young, L. Xiong, K. Fezzaa, W. Everhart, B. Brown, T. Sun, L. Chen, et al., Transient dynamics of powder spattering in laser powder bed fusion additive manufacturing process revealed by in-situ high-speed high-energy x-ray imaging, Acta Mater. 151 (2018) 169–180, doi:10.1016/j.actamat.2018.03.036.
[8] P. Bidare, I. Bitharas, R.M. Ward, M.M. Attallah, A.J. Moore, Fluid and particle dynamics in laser powder bed fusion, Acta Mater. 142 (2018) 107–120, doi:10.1016/j.actamat.2017.09.051.
[9] S.A. Khairallah, A.T. Anderson, A.M. Rubenchik, W.E. King, Laser powder-bed fusion additive manufacturing physics of complex melt flow and formation mechanisms of pores, spatter, and denudation zones, in: Additive Manufacturing Handbook, 2017, pp. 613–625, doi:10.1201/9781315119106-33.
[10] C. Pauzon, B. Hoppe, T. Pichler, S. Dubiez-Le Goff, P. Forêt, T. Nguyen, E. Hryha, Reduction of incandescent spatter with helium addition to the process gas during laser powder bed fusion of ti-6al-4v, CIRP J. Manuf. Sci. Technol. 35 (2021) 371–378, doi:10.1016/j.cirpj.2021.07.004.
[11] S.A. Khairallah, A.A. Martin, J.R. Lee, G. Guss, N.P. Calta, J.A. Hammons, M.H. Nielsen, K. Chaput, E. Schwalbach, M.N. Shah, et al., Controlling interdependent meso-nanosecond dynamics and defect generation in metal 3D printing, Science 368 (6491) (2020) 660–665, doi:10.1126/science.aay7830.
[12] J. Yin, W. Zhang, L. Ke, H. Wei, D. Wang, L. Yang, H. Zhu, P. Dong, G. Wang, X. Zeng, et al., Vaporization of alloying elements and explosion behavior during laser powder bed fusion of cu–10zn alloy, Int. J. Mach. Tools Manuf 161 (2021) 103686, doi:10.1016/j.ijmachtools.2020.103686.
[13] P. Deng, M. Karadge, R.B. Rebak, V.K. Gupta, B.C. Prorok, X. Lou, The origin and formation of oxygen inclusions in austenitic stainless steels manufactured by laser powder bed fusion, Addit. Manuf. 35 (2020) 101334, doi:10.1016/j.addma.2020.101334.
[14] D. Wang, S. Wu, F. Fu, S. Mai, Y. Yang, Y. Liu, C. Song, Mechanisms and characteristics of spatter generation in SLM processing and its effect on the properties, Mater. Des. 117 (2017) 121–130, doi:10.1016/j.matdes.2016.12.060.
[15] K.A. Mumtaz, N. Hopkinson, Selective laser melting of thin wall parts using pulse shaping, J. Mater. Process. Technol. 210 (2) (2010) 279–287, doi:10.1016/j.jmatprotec.2009.09.011.
[16] V. Gunenthiram, P. Peyre, M. Schneider, M. Dal, F. Coste, I. Koutiri, R. Fabbro, Experimental analysis of spatter generation and melt-pool behavior during the powder bed laser beam melting process, J. Mater. Process. Technol. 251 (2018) 376–386, doi:10.1016/j.jmatprotec.2017.08.012.
[17] X. Zhang, J.H. Rao, M. Wang, B. Cai, H. Liu, Structural design of a novel fume hood for vapor and spatter removal in direct energy deposition via numerical investigation, Addit. Manuf. 37 (2021) 101704, doi:10.1016/j.addma.2020.101704.
[18] C. Tenbrock, T. Kelliger, N. Praetzsch, M. Ronge, L. Jauer, J.H. Schleifenbaum, Effect of laser-plume interaction on part quality in multi-scanner laser powder bed fusion, Addit. Manuf. 38 (2021) 101810, doi:10.1016/j.addma.2020.101810.
[19] M. Yakout, I. Phillips, M.A. Elbestawi, Q. Fang, In-situ monitoring and detection of spatter agglomeration and delamination during laser-based powder bed fusion of invar 36, Opt. Laser Technol. 136 (2021) 106741, doi:10.1016/j.optlastec.2020.106741.
[20] C.L.A. Leung, S. Marussi, R.C. Atwood, M. Towrie, P.J. Withers, P.D. Lee, In situ X-ray imaging of defect and molten pool dynamics in laser additive manufacturing, Nat. Commun. 9 (1) (2018) 1355, doi:10.1038/s41467-018-03734-7.
[21] E. Eschner, T. Staudt, M. Schmidt, 3D particle tracking velocimetry for the determination of temporally resolved particle trajectories within laser powder bed fusion of metals, Int. J. Extreme Manuf. 1 (2019) 035002, doi:10.1088/2631-7990/ab3de9.
[22] D. Dabiri, C. Pecora, Particle Tracking Velocimetry, IOP Publishing, 2020.
[23] E.H. Adelson, J.Y.A. Wang, Single lens stereo with a plenoptic camera, IEEE Trans. Pattern Anal. Mach. Intell. 14 (2) (1992) 99–106, doi:10.1109/34.121783.
[24] R. Ng, M. Levoy, G. Duval, Light Field Photography with a Hand-held Plenoptic Camera, Stanford Tech Report, 2005, doi:10.1109/MC.2006.270.
[25] Z.P. Tan, K. Johnson, C. Clifford, B.S. Thurow, Development of a modular, high-speed plenoptic-camera for 3D flow-measurement, Opt. Express 27 (9) (2019) 13400, doi:10.1364/oe.27.013400.
[26] H.G. Maas, A. Gruen, D. Papantoniou, Particle tracking velocimetry in three-dimensional flows, Exp. Fluids 15 (2) (1993) 133–146.
[27] T. Keya, V. O'Donnell, J. Lieben, A. Romans, G. Harvill, M. Andurkar, J. Gahl, S.M. Thompson, B.C. Prorok, et al., Effects of Heat Treatment and Fast Neu-

tron Irradiation on the Microstructure and Microhardness of Inconel 625 Fabricated via Laser-Powder Bed Fusion, University of Texas at Austin, 2021, doi:10.26153/tsw/17625. Accepted: 2021-12-06T22:54:26Z
[28] E.A. Deem, Y. Zhang, L.N. Cattafesta, T.W. Fahringer, B.S. Thurow, On the resolution of plenoptic PIV, Meas. Sci. Technol. 27 (8) (2016) 084003, doi:10.1088/0957-0233/27/8/084003.
[29] T.W. Fahringer, K.P. Lynch, B.S. Thurow, Volumetric particle image velocimetry with a single plenoptic camera, Meas. Sci. Technol. 26 (11) (2015) 115201, doi:10.1088/0957-0233/26/11/115201.
[30] A. Lab, Prana, 2015, (https://github.com/aether-lab/prana).
[31] E.A. Cowen, S.G. Monismith, A hybrid digital particle tracking velocimetry technique, Exp. Fluids 22 (3) (1997) 199–211.
[32] M. Levoy, Light fields and computational imaging, Computer 39 (8) (2006) 46–55, doi:10.1109/MC.2006.270.
[33] C. Clifford, Z. Tan, E. Hall, B. Thurow, Particle matching and triangulation using light-field ray bundling, 13th International Symposium on Particle Image Velocimetry (2019).
[34] E.M. Hall, T.W. Fahringer, D.R. Guildenbecher, B.S. Thurow, Volumetric calibration of a plenoptic camera, Appl. Opt. 57 (4) (2018) 914, doi:10.1364/ao.57.000914.
[35] A. Clark, N. Machicoane, A. Aliseda, A quantitative study of track initialization of the four-frame best estimate algorithm for three-dimensional lagrangian particle tracking, Meas. Sci. Technol. 30 (4) (2019) 045302, doi:10.1088/1361-6501/ab0786.
[36] D. Schanz, S. Gesemann, A. Schröder, Shake-the-box: Lagrangian particle tracking at high particle image densities, Exp. Fluids 57 (5) (2016), doi:10.1007/s00348-016-2157-1.
[37] C. Barrett, C. Carradero, E. Harris, K. Rogers, E. MacDonald, B. Conner, Statistical analysis of spatter velocity with high-speed stereovision in laser powder bed fusion, Prog. Addit. Manuf. 4 (4) (2019) 423–430, doi:10.1007/s40964-019-00094-6.
[38] J. Yin, L. Yang, X. Yang, H. Zhu, D. Wang, L. Ke, Z. Wang, G. Wang, X. Zeng, High-power laser-matter interaction during laser powder bed fusion, Addit. Manuf. 29 (2019) 100778, doi:10.1016/j.addma.2019.100778.
[39] A. Lumsdaine, T. Georgiev, The focused plenoptic camera, in: 2009 IEEE International Conference on Computational Photography (ICCP), 2009, pp. 1–8, doi:10.1109/ICCPHOT.2009.5559008.